A New Approach Towards Measuring Structure Factors and Valence-Electron Distribution in Crystals with Large Unit Cells

J. Taftø,*† Yimei Zhu and Lijun Wu

Materials Science Division, Department of Applied Science, Brookhaven National Laboratory, Upton, NY 11973, USA. E-mail: johan.tafto@fys.uio.no

Abstract

By focusing a probe of fast electrons above or below the specimen level in convergent-beam electron diffraction, shadow images of many reflections are recorded in one exposure. For wedge-shaped crystals, this procedure provides a means of recording thickness or *Pendellösung* fringes of many reflections simultaneously, which ensures that the experimental conditions with respect to thickness variations and crystallographic direction of the incident beam are the same for all reflections. Disturbing defects within the illuminated area of the specimen are immediately revealed in the shadow images of the different reflections. The approach is introduced by using strontium titanate and silicon as examples. As a case study, the technique is applied to the dense $(00l)$ reciprocal-lattice row of the superconductor $YBa_2Cu_3O_7$ to address charge transfer and electron-hole distribution by determining the amplitudes and phases of the 001 and 002 reflections. By this approach, the absolute values of the structure factors are obtained from the very thin regions where the kinematical theory applies. Based on these approximate absolute values, the signs of the structure factors in centrosymmetrical crystals are determined by comparing dynamically calculated and observed intensities in somewhat thicker crystal regions for different combinations of signs. As a third step, the structure factors are refined by comparing the calculated and experimental intensity profiles within the entire observed thickness range.

1. Introduction

Diffraction experiments with 100–1000 keV electrons have great potential capabilities for crystallographic studies, see Spence (1993) and Tanaka (1994) for reviews. An example is the possibility of locating accurately the atoms in the crystal unit cell because of the short wavelength that ranges from 4 to 1 pm for these fast electrons. Another important issue is the distribution of valence electrons in materials, which can be

addressed because of the very high sensitivity to charge transfer at small scattering angles in electron diffraction, *i.e.* at low-index reflections in large-unit-cell crystals. The reason for this is that the incident electrons interact with the electrostatic potential, which includes contributions from the positive charges of nuclei in addition to the negative charges of the electrons in the crystal. This opens up the possibility of studying ionicity, bonding and valence-electron distribution in large-unit-cell crystals as pointed out by Cowley (1953), studied in great detail by Anstis *et al.* (1973) and recently applied to high-temperature superconductors by Gjønnes *et al.* (1993) and Zhu & Taftø (1996, 1997). Furthermore, electron diffraction can be applied to very small volumes of materials to study the regions around point, line and planar defects and individual nanocrystals of size down to a few nm. This capability is tied to the high brightness of the electron source and the fact that an electron beam is easily focused. Thus, an electron probe of very high brilliance can be confined to nanometer-sized areas on or near the specimen.

Despite these advantages, electron diffraction has been inferior to X-ray and neutron diffraction as a quantitative technique for accurate crystallographic studies. A major challenge has been to record quantitatively the electron diffraction intensities. In addition, the strong interaction between electrons and matter results in strong elastic and inelastic scattering and thus dynamical effects and considerable absorption down to small thicknesses. These same dynamical effects have been used advantageously to determine the amplitudes and phases of structure factors for inner reflections of small-unit-cell crystals, typically reflections corresponding to interplanar spacings between 0.15 and 0.45 nm. Techniques that have been commonly used for small-unit-cells crystals are *Pendellösung* fringes (Ichimiya & Uyeda, 1977), the critical-voltage (CV) method (Watanabe *et al.*, 1968) and the intersecting Kikuchi-line (IKL) technique (Gjønnes & Høier, 1971). The CV technique relies on dynamical extinction of a certain reflection at a particular incident-beam energy, while with the IKL technique attention is focused on certain features in the Kikuchi pattern. In the last two decades, convergent-beam electron diffraction (CBED)

---

† Visiting scientist from the Department of Physics, University of Oslo, PO Box 1048, Blindern, N-0316 Oslo, Norway.

has replaced conventional Kikuchi patterns for these purposes (Marthinsen & Høier, 1988; Zuo *et al.*, 1989), recently in combination with energy filtering to highlight and quantify the features of the CBED patterns (Zuo & Spence, 1991). By automation of the fitting process, simulated CBED patterns are compared with observed patterns for accurate determination of structure factors (Zuo, 1993). Such quantitative CBED studies with high precision can now be used to extract important information about bonding and ionicity in small-unit-cell crystals (Zuo *et al.*, 1988; Matsuhata *et al.*, 1994; Zuo *et al.*, 1997).

A somewhat different approach is to use very thin crystals, of the order of 10 nm thick (Burshill *et al.*, 1974; Olsen *et al.*, 1985). For such thin crystals, electron diffraction is less dynamical and the interpretation procedure becomes simpler. With a small convergence of the incident beam, this approach is suited to crystals with large unit cells but control of the thickness of the crystal is critical and, thus, the method works best on thin platelet-shaped crystals. Here this technique is modified so that we can observe the intensity variation with thickness in wedge-shaped crystal areas. We do this in CBED by focusing the electron beam above or below the specimen level. Thus, each convergent-beam reflection, the so-called disc, becomes a shadow image of the illuminated area of the specimen and many thickness or *Pendellösung* fringes can be recorded
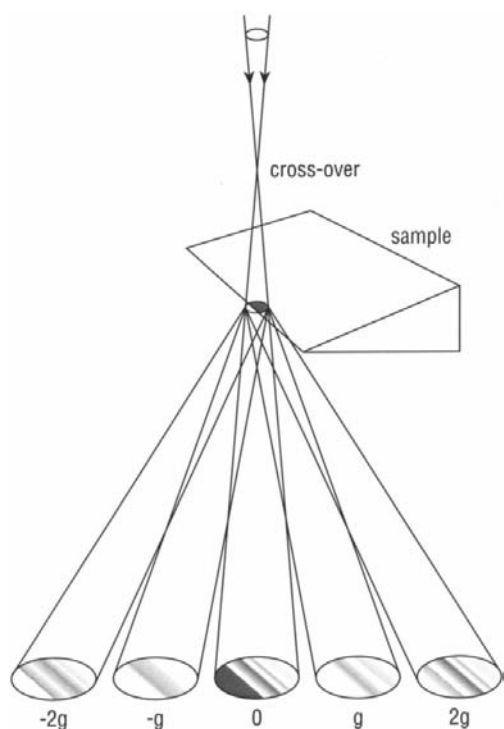
simultaneously. Shadow images, obtained in the diffraction mode, have previously been used to study defects and strain near interfaces in materials (Burshill *et al.*, 1974; Cherns *et al.*, 1988). These patterns contain real-space coordinates in addition to reciprocal coordinates.

2. Experiment and information content

Diffraction data at a certain crystal thickness, varying continuously with incident-beam direction within the limits set by the condenser aperture, are acquired in an ideal conventional CBED experiment with a very small probe focused on the specimen. The incident-beam directions within a CBED disc are determined by the crystal orientation in the specimen holder and the size of the condenser aperture. For certain purposes, the electron probe has previously been focused at heights different from the specimen level (Burshill *et al.*, 1974; Tanaka *et al.*, 1980; Vincent *et al.*, 1984; Humphreys *et al.*, 1988; Cherns *et al.*, 1988; Duan *et al.*, 1994). A larger area of the crystal is then illuminated as shown in Fig. 1. The information content is the same with a focused and defocused probe on the specimen when, and only when, the crystal is perfect, the crystal planes flat (no bending) and the thickness constant over the illuminated area. By focusing the probe in the plane of the selected-area aperture, a large-angle CBED disc of one of the reflections can be separated from overlapping discs by inserting the aperture to block the other discs (Tanaka *et al.*, 1980). If the diffraction discs do not overlap, focusing at any level may give useful information and spatial resolution from crystals with defects and thickness variations is present if the crossover is above or below the specimen level. Focusing at a level different from the specimen level has been used to form shadow images of areas with extended defects by *e.g.* Burshill *et al.* (1974). We have taken similar shadow images at 200 keV and some of them are shown in Fig. 2. Note that there is one bright-field and as many dark-field images as there are reflections in the diffraction pattern. For a bent specimen, it is thus possible to record the bend contours of many reflections simultaneously as shown in Figs. 2(*a*) and (*b*). These patterns are from a strongly buckled thin area of $SrTiO_3$. However, more important from a crystallographic point of view is the simultaneous presence of the bright-field and dark-field *Pendellösung* fringes from non-bent crystals which are wedge-shaped at the edge as shown in Figs. 2(*c*) and (*d*). The *Pendellösung* fringes in Figs. 2(*c*) and (*d*) are from an Si specimen. The **g** vector is normal to the edge of the wedge in Fig. 2(*c*) and parallel to the edge in Fig. 2(*d*). In Fig. 2(*d*), with the **g** vector parallel to the edge of the wedge, the period of the intensity oscillations normal to the wedge scales with the extinction length. In the two-beam approximation, the intensity distribution in the dark-field and bright-
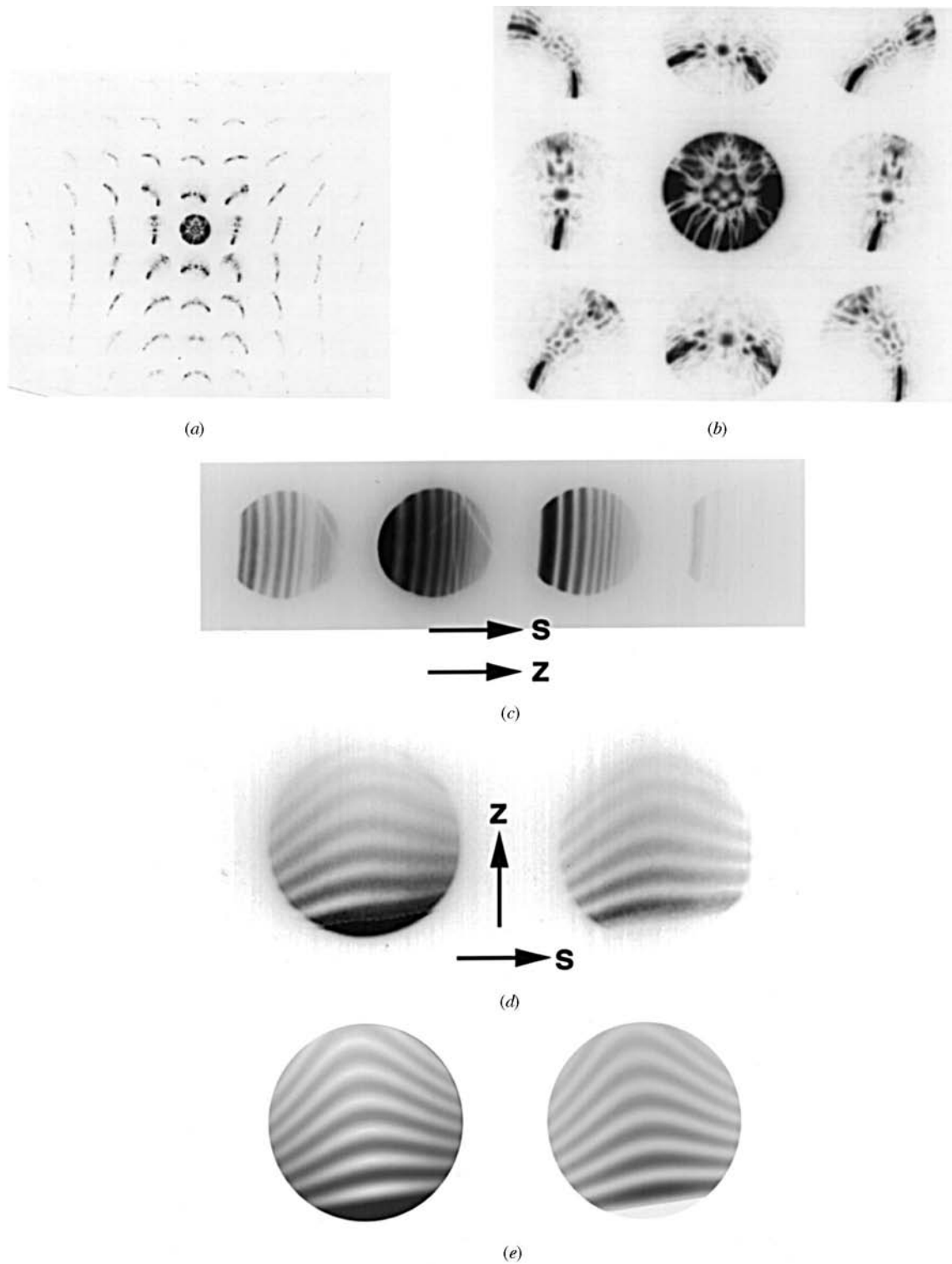

Fig. 1. Schematics of the experimental set-up to obtain shadow image diffraction patterns.

Fig. 2. Shadow image diffraction. (*a*) and (*b*) from a thin heavily bent (001) foil of SrTiO$_3$ at two different camera lengths. (*c*) and (*d*) are from a wedge-shaped area of Si showing the (00*l*) reciprocal row and 000 and 220 diffraction discs, respectively. The edge in (*c*) and (*d*) is normal and parallel to the **g** vector, respectively. (*e*) shows the two-beam calculated intensity maxima in the bright-field and dark-field discs.

field images as a function of thickness, z, and excitation error, s_g, can be expressed by:

$$I_g = 1 - I_0 = [1/1 + (Ks_g/U_g)^2]$$
$$\times \sin^2 \left\{ \frac{\pi z [1 + (Ks_g/U_g)^2]^{1/2}}{K/U_g} \right\}. \quad (1)$$

Here, K is the wave vector of the incident electrons modified by the mean inner potential of the crystal and $U_g = (m_{rel}/m_e)(F_g^e/\pi V_c)$ the relativistically corrected Fourier component of the electrostatic potential for reflection g. m_e, m_{rel}, F_g^e and V_c are the rest mass of the electron, the relativistic mass of the electron, the structure factor for electron diffraction and the volume of the crystal unit cell, respectively. s_g, which is the excitation error, can be written:

$$s_g = (2\mathbf{c} \cdot \mathbf{g} - \mathbf{g}^2)/2K, \quad (2)$$

where the crystallographic direction of the incident beam is expressed by the coordinate of the center of the Laue circle, $\mathbf{c}$, i.e. the component of the incident beam onto the projection under consideration. Absorption is neglected in (1). From (1), we can, in the two-beam approximation, easily simulate the intensity variations within the CBED discs when the crystallographic direction of the incident beam, the wedge angle and the structure factor are known. In Fig. 2(e), two-beam calculations with absorption are compared with experimental observations for the 220 reflection of Si shown in Fig. 2(d). We did not know the wedge angle in this case and have used a thickness scale that gives qualitative agreement with the observation. In the diffraction pattern of Fig. 2(d), the axes of thickness and excitation error are orthogonal to each other, while these parameter axes are parallel in Fig. 2(c). In general, for a wedge, there is in the pattern an angle φ between the thickness axis, z, and the excitation error axis, s. When the thickness profile of the illuminated volume of the specimen deviates from that of a perfect wedge and the crystal is bent over the illuminated area, the (z, s) plane becomes distorted. An extreme example of such distortions was demonstrated in Figs. 2(a) and (b). Patterns, such as those from Si in Fig. 2(d), could probably have been used for accurate determination of structure factors in small-unit-cell crystals because of the ability to record the extinction contours and thickness fringes simultaneously and thereby combine the thickness fringe and the conventional CBED method. These two methods have been used separately for accurate structure-factor measurements (Ichimiya & Uyeda, 1977; Zuo et al., 1989).

Our priority, however, is large-unit-cell crystals where the amplitudes and the phases of the inner reflections are very sensitive to the charge distribution. We address the charge distribution along the c axis in a fully oxygenated sample of the high-T_c superconductor YBa$_2$Cu$_3$O$_7$. With the long repeat unit of $c = 1.168$ nm, we record many reflections simultaneously along the $(00l)$ reciprocal row (Fig. 3). We thus achieve parallel recording of oscillating diffraction intensities (PARODI) as a function of thickness and excitation error for many reflections. PARODI can be used on very small crystal areas and the thickness profiles of many reflections are recorded in one exposure. In Fig. 3(a), the angle φ between the c axis and the edge of the wedge is about 45°. The observation of no significant variation in the intensity parallel to the edge within the individual discs suggests in this case, with a small convergence angle and all recorded reflections at rather small scattering angles, that there is little variation in intensity within the small range of excitation errors represented by the CBED discs. Thus, in principle, for such dense reciprocal-lattice rows near symmetrical incidence, the orientation of the edge of the wedge relative to the reciprocal-lattice row is unimportant but the pattern is most conveniently digitized with a scanner when the edge is normal to the reciprocal-lattice row as shown in Fig. 3(b). Then, in a single scan, we obtain thickness profiles of many reflections as shown in Fig. 3(c). By focusing the beam on the specimen to form conventional CBED patterns (Fig. 4), the CBED discs are rather uniformly filled but the distribution of intensities between the reflections varies greatly from one CBED pattern to the next owing to small changes in thickness. This was a problem encountered by the electron diffraction group at CSIRO who for more than two decades has successfully used such patterns to study large-unit-cell crystals and they have stressed the challenge of thickness determination in several papers (Anstis et al., 1973; Burshill et al., 1974). The problem occurs, in particular, for ionic crystals with large unit cells where the inner reflections may be very strong
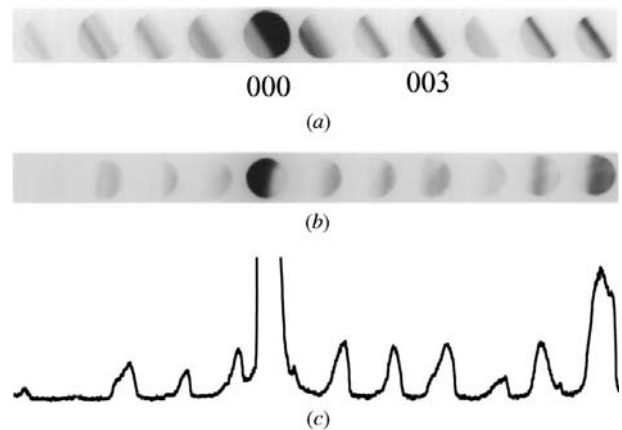

Fig. 3. Parallel recording of the oscillating intensities, PARODI, of the $(00l)$ reciprocal row of YBa$_2$Cu$_3$O$_7$, with angles of about 45 and 90° between the $(00l)$ row and the edge in (a) and (b), respectively. (c) is a scan of (b).

owing to charge transfer, resulting in strong coupling and, thus, rapid oscillations of the intensities of the Bragg beams with thickness (Anstis *et al.*, 1973). The conventional CBED patterns from the thin areas of the superconductor in Figs. 4(*a*) and (*b*) demonstrate this great change of the diffraction patterns with small changes in thickness. From the PARODI patterns in Figs. 3(*a*) and (*b*), where the thickness is estimated to range from 0 to 60 nm and 0 to 15 nm, respectively, we realize immediately that conventional CBED patterns become very different even after small changes in thickness. The depth definition of PARODI patterns, *i.e.* resolution of the thickness fringes, depends on the spot size at crossover and the wedge angle, while the magnification depends on the camera length and the distance from the crossover to the specimen.

The electron diffraction intensities are nearly kinematical when the crystal thickness is smaller than about 5–10 nm (Burshill *et al.*, 1974) and thus the absolute values of the structure factors for several reflections may be retrieved from the thin region of a single PARODI exposure, while information about the phases of the structure factors is present in the areas of the shadow image representing the thicker regions of the sample where the dynamical coupling between the beams comes into play. In the case of centrosymmetric crystals, the experimental thickness fringes can be compared with dynamical calculations by trying different combinations of positive and negative values of the signs of the structure factors. This is the procedure we pursue to address the ionicity and the electron-hole distribution in the centrosymmetric $YBa_2Cu_3O_7$.

3. Interpretation of the experimental data

3.1. *General*

A brief account of the application of PARODI to locate the electron holes in $YBa_2Cu_3O_7$ was presented in a recent paper (Zhu & Taftø, 1997). We here present a more comprehensive and general interpretation procedure. Our major aim is to determine the amplitudes and phases of reflections with short **g** vectors and we believe

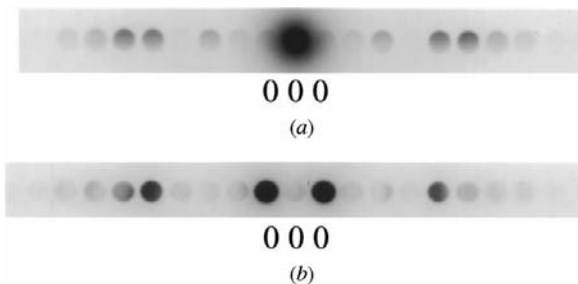**0 0 0**

(*a*)

0 0 0

(*b*)

Fig. 4. Conventional convergent-beam diffraction patterns of two areas estimated to be (*a*) 10 nm and (*b*) 45 nm thick. Note also here intensity variations within the discs because of the steep wedge.

the approach presented here has the potential of becoming a rather general procedure. Thus, we will describe in some detail how amplitudes and phases of structure factors can be retrieved from these experiments where the intensities of many reflections are experimentally recorded simultaneously from zero thickness up to thicknesses of several hundred nm. Although the study of charge transfer in high-temperature superconductors is important *per se*, this presentation is meant as a case study to serve as an example for future studies of large-unit-cell crystals in general. The ultimate goal is to determine the spatial distribution of valence electrons in crystals with large unit cells and, in particular, for high-temperature superconductors to determine the distribution of the electron holes that are the charge carriers, see *e.g.* Pickett (1989).

Before we start with the interpretation, let us look at how to extract the electron distribution in a crystal from the Fourier components of the electrostatic potentials, which is what is measured in electron diffraction experiments.

The relationship between the atomic scattering amplitude for X-rays and electrons is, according to the Mott formula for the electron scattering amplitude in SI units:

$$f^e(\theta) = (m_e e^2 / 8\pi\varepsilon_o h^2)(\lambda/\sin\theta)^2(Z - f^x). \qquad (3)$$

Here Z is the number of positive elementary charges in the nucleus and f^x, which is the scattering amplitude of the ion for incident X-rays, is the Fourier transform of the spatial distribution of electrons around the nucleus.

The structure factor for X-ray diffraction is

$$F_g^x = \sum_i f_i^x(s) \exp(-2\pi i \mathbf{g} \cdot \mathbf{r}) \exp(-B_i s^2). \qquad (4)$$

B_i is the Debye–Waller factor of the ith atom and $s = \sin\theta/\lambda$.

Similarly, for electron diffraction:

$$F_g^e = \sum_i f_i^e(s) \exp(-2\pi i \mathbf{g} \cdot \mathbf{r}) \exp(-B_i s^2). \qquad (5)$$

Note that the electron structure factor parallels the X-ray structure factor by replacing the atomic scattering amplitude for X-rays by the scattering amplitude for electron scattering, f^e, as expressed in (3).

When the X-ray structure factors are known, the electron charge distribution is found from the relationship

$$\rho(r) = \sum_g F_g^x \exp(-2\pi i \mathbf{g} \cdot \mathbf{r}). \qquad (6)$$

Similarly, for electron diffraction, the electrostatic potential in the crystal is given by

$$U(r) = \sum_g U_g^0 \exp(-2\pi i \mathbf{g} \cdot \mathbf{r}). \qquad (7)$$

In U_g^0, the superscript is introduced to specify that this is the Fourier coefficient of the electrostatic potential rather than the relativistically corrected one. The latter is used in the dynamical calculations, as seen in (1). Furthermore, the structure factor for electron diffraction, F_g^e, is related to the Fourier coefficients, U_g^0, of the electrostatic potential by $U(r)$ by:

$$(m_e/m_{rel})U_g = U_g^0 = F_g^e/\pi V_c. \qquad (8)$$

Here, V_c is the volume of the crystal unit cell.

We are aiming at determining the electron distribution in the crystal from electron diffraction data by converting F_g^e to F_g^x before performing the Fourier transform using (6). The conversion is done by combining (3), (4) and (5):

$$F_g^x = \left[\sum_i Z_i \exp(-B_i s^2) \exp(-2\pi i \mathbf{g} \cdot \mathbf{r}) \right] - (c_1 s^2 F_g^e). \qquad (9)$$

Here, $c_1 = 8\pi\varepsilon_0 h^2/m_e e^2 = 41.78 \text{ Å e}$.

We determine the structure factors in three steps, starting with the experimental determination of the amplitudes of the low-order reflections by focusing attention on the onset of intensity increase in the thin crystal region where the kinematical approximation is reasonably good and where the intensity scales with the square of the thickness. We then proceed, by a trial-and-error procedure, to determine those phases of structure factors that are unknown. This is done in dynamical calculations of the diffraction intensities by combining positive and negative signs that are the only alternatives in this centrosymmetric crystal. As the third step, we refine the amplitudes of the Fourier potentials by comparing calculated intensity profiles for successive changes of the amplitudes until we obtain a good fit within the entire observed thickness range. Finally, we Fourier transform the experimentally determined Fourier potentials to estimate the spatial variation of the electrostatic potential and electron charge distribution.

3.2. Estimation of the amplitude of the 001 and 002 reflections

For a very thin crystal where the kinematical theory can be used, the relationship between the Fourier potential U_g of reflection g, the intensity, I_g, and the thickness of the crystal, z, is given by

$$I_g = \pi^2 z^2 U_g^2/K^2. \qquad (10)$$

This is a well known result that can be deduced from (1) in the limit of thin crystal, i.e. small z. This relationship is, within reasonable limits, independent of the incident-beam direction as shown in Fig. 5 where the intensities of the reflections along the 001 row of $YBa_2Cu_3O_7$ are calculated dynamically for two different incident-beam directions. The component of the wave vector of the

incident electrons along the 00l row is zero in Fig. 5(a) and 003 in Fig. 5(b). This means symmetrical incidence and the 006 reflection at the Bragg position, respectively. In these calculations, and those of Fig. 5(c) for a thicker specimen, we have assumed neutral atoms and we used
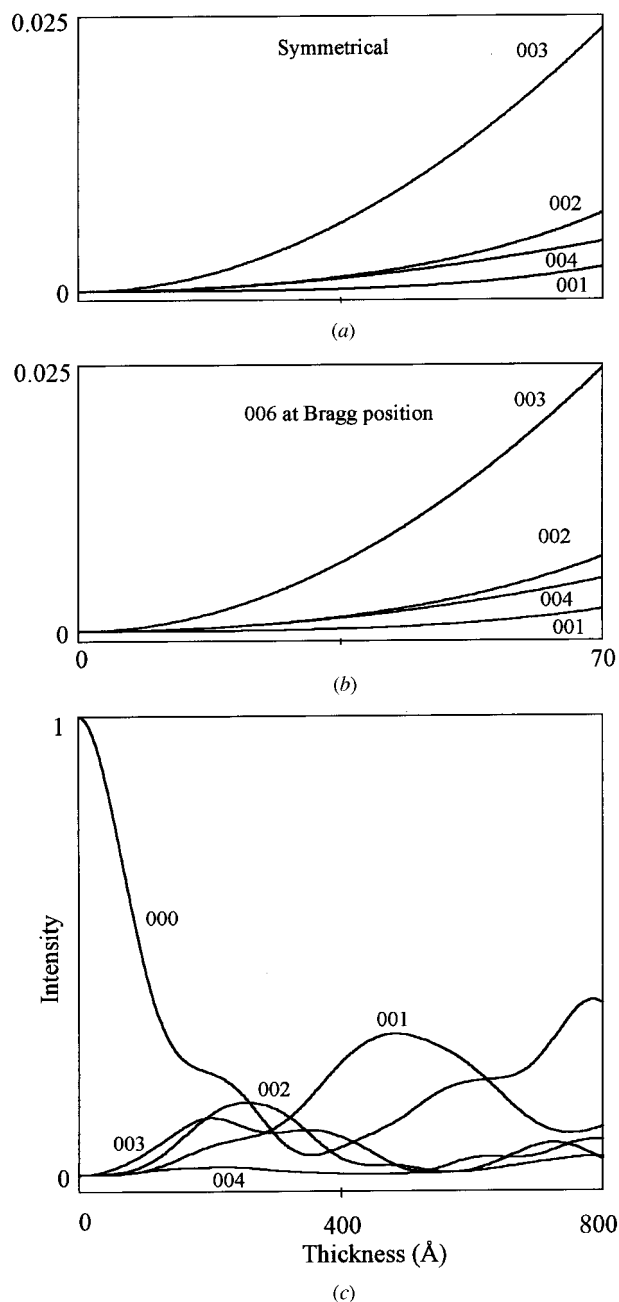

Fig. 5. Calculations of intensity variations with thickness for the (00l) row in $YBa_2Cu_3O_7$ assuming neutral atoms. (a) and (b) are from very thin regions for symmetrical incidence and 006 reflection at the Bragg position, respectively. Note that in these thin regions the intensity profiles are barely influenced by the incident-beam direction. (c) Calculations up to larger thicknesses (800 Å) for symmetrical incidence.

the atomic positions of $YBa_2Cu_3O_7$ determined by Jorgensen *et al.* (1990) by powder neutron diffraction. The crystal unit cell of the fully oxygenated sample of $Yba_2Cu_3O_7$ contains one formula unit and is ortho-rhombic with volume $V_c = abc = 0.382 \times 0.388 \times 1.168$ nm $= 0.173$ nm^3. We used the X-ray scattering amplitudes tabulated in *International Tables for Crystallography* (1992). These were converted to scattering amplitudes for electrons using (3). The structure factors were calculated with the origin chosen in the CuO chain. Dynamical calculations were performed with both multislice and Bloch-wave computer programs. These quite different calculation procedures gave essentially the same results and here we present the results of the Bloch-wave calculations obtained by including 51 reflections along the $00l$ reciprocal-lattice row. The

calculations for the two different incident-beam directions shown in Figs. 5(*a*) and (*b*) support the idea that we can estimate the absolute values of the structure factors from the thin crystal regions and, from the observations in the thin area of Fig. 3, we find that the intensities of the 001 and 002 reflections are both about one quarter of the intensity of the 003 reflection near the onset at zero thickness, which means according to (10) that the amplitudes of the 001 and 002 reflections are approximately one half of the amplitude of the 003 reflection.

3.3. *Dynamical calculations for phase determination*

With reference to (3), only the 001 and possibly, but less likely, the 002 reflections are influenced by the charge distribution to the extent that we cannot predict
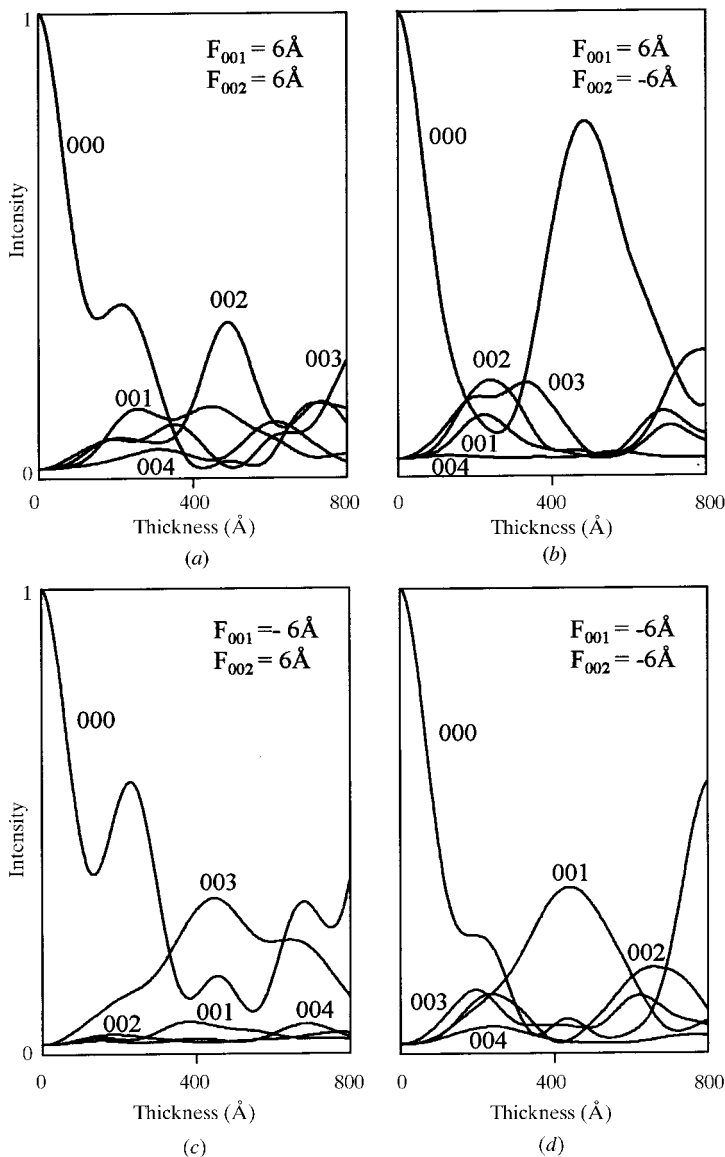

Fig. 6. Calculations of the intensity as a function of thickness for symmetrical incidence based on the estimated absolute values of the structure factors of the 001 and 002 reflections and for the four combinations of the signs of the structure factors.

their phases from the known atomic coordinates. The structure factors of the reflections further out along the (00l) row are mainly determined by the positions of the atoms. Thus, because the crystal is centrosymmetric, there are four possible outcomes with respect to phase combinations if we imagine that, in addition to the 001 reflection, the 002 reflection could also change sign by rearrangement of the electron charge in the crystal unit cell. For these four combinations, we perform dynamical calculations of the intensity variation with thickness (Fig. 6), under the assumption that the absolute value of the structure factors of the 001 and 002 reflections are both 6 Å, *i.e.* half the absolute value of the structure factor of the 003 reflection, which was calculated to be −12 Å. Also, these calculations were performed using the Bloch-wave program and 51 beams along the (00l) reciprocal row. Only the choice of negative sign for both the 001 and 002 reflections (Fig. 6d) gives reasonable agreement with the observed intensity profiles. This may be most directly seen by comparing with the conventional CBED pattern of Fig. 4(b) at an estimated thickness of 45 nm. This thickness estimation relied on comparing the observed PARODI patterns with calculated intensities in the whole thickness range seen in PARODI patterns such as those of Fig. 3. Note that, at the estimated thickness of 45 nm, the 001 reflection is observed to be strong while the 000, 002, 003 and 004 reflections are very weak, in agreement with the calculations for negative values of the 001 and 002 structure factors in Fig. 6(d).

3.4. *Refinement of the structure factors of the 001 and 002 reflections*

At the present stage, we lack a perfect wedge and there are possibilities of distortions and even deviation from the bulk charge distribution in the very thin areas
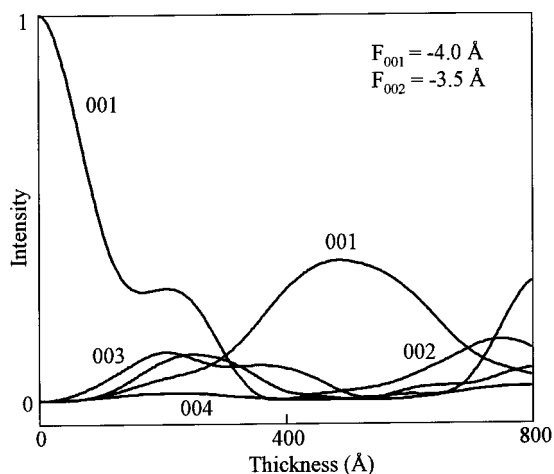
but such irregularities can fortunately be revealed by the requirement of internal consistency between the thickness fringes from thin and thicker regions of the PARODI patterns. We refined the amplitudes of the 001 and 002 reflections by systematically changing these amplitudes in the calculations until we obtained the best agreement with observation. In Fig. 7, we show the calculated PARODI for symmetrical incidence for the best combination of values of the structure factors of the 001 and 002 reflections. In this refinement, the values of the structure factors of the 001 and 002 reflections were found to be −4.0 and −3.5 Å, respectively. A more detailed comparison of calculated intensity profiles, based on these values of the structure factors, with experimental intensity scans of PARODI patterns are shown in Fig. 8 where the 006 reflection is at the Bragg position.

3.5. *Fourier transform of the experimental data and conversion to electron distribution along the c direction in the crystal*

From the determined values of the 001 and 002 structure factors, we calculate the difference between the measured electrostatic potential U_m and the one to be expected for neutral atoms, U_n. The structure factors of 001 and 002 for neutral atoms were found to be −1.2 and −4.9 Å by using the atomic coordinates and Debye–Waller factor of Jorgensen *et al.* (1990) and the atomic scattering amplitudes for electron diffraction obtained by conversion from the ones for X-ray diffraction (*International Tables for Crystallography*, 1992). Our intention is now to extract the change in electrostatic potential $\Delta U(\mathbf{r})$ and charge density $\Delta\rho(\mathbf{r})$ owing to charge transfer relative to neutral atoms:

$$\Delta U(\mathbf{r}) = U_m(\mathbf{r}) - U_n(\mathbf{r})$$
$$= (m_e/m_{\rm rel}) \sum (U_{gm} - U_{gn}) \exp(-2\pi i \mathbf{g} \cdot \mathbf{r}). \quad (11)$$

Along the c direction, where we have observed only the 001 and 002 reflections to be significantly influenced by electron redistribution, we have

$$\Delta U(Z) = 2(m_e/m_{\rm rel})[(U_{001m} - U_{001n})\cos 2\pi Z$$
$$+ (U_{002m} - U_{002n})\cos 4\pi Z]. \quad (12)$$

We can convert from electron to X-ray structure factors and calculate $\Delta\rho$ analogously. The conversion from U_g to F_g^x is achieved by using (9) for the relationship between the X-ray structure factors and the Fourier potentials. Because we are considering only reflections at very low scattering angles, the attenuating term due to the thermal vibrations in (9) can be neglected. The difference between the measured charge distribution and the charge distribution assuming neutral atoms is obtained by replacing $U_g m_e/m_{\rm rel}$ by F_g^x in (12).

Fig. 7. A choice of values of the 001 and 002 structure factors that give good agreement with the observed intensity profiles.

4. Discussion

Comparisons between observed intensity profiles and those calculated with different combinations of signs of the 001 and 002 structure factors as shown in Fig. 6 leave little doubt that the signs of these two structure factors in electron diffraction are both negative. At present, the accuracy in the determined values of the structure factors, even after refinement, is rather modest, but after conversion to X-ray structure factors, those at small scattering angles become very accurate. Our estimates of the accuracy of the 001 and 002 structure factors of electron diffraction are 1.0 Å and thus the structure factors are $-4.0\,(1)$ and $-3.5\,(1)$ Å, respectively. This accuracy is estimated based on comparisons between the observations and calculations of the thickness intensity profiles for many different combinations of values of these two structure factors. After conversion to structure factors for X-ray diffraction, we get $F^x_{001m} - F^x_{001n} = 0.22$ e and $F^x_{002m} - F^x_{002n} = -0.5$ e. Based on these residuals, $\Delta\rho$ is plotted in Fig. 9. We note a considerable deficiency of valence electrons in the region around the Y atom as is expected from considerations of formal valency. At present, we are not able to observe a significant difference between the measured and calculated structure factors for reflections in reciprocal space further out than the 002 reflection and thus the spatial resolution of the valence-electron distribution is rather poor.

Sensible information about the electronic structure from diffraction experiments relies on contrasting, in either real or reciprocal space, the experimentally determined charge distribution with the charge distribution calculated assuming neutral or ionized atoms or by comparing with electronic structure calculations. The hole distribution in $YBa_2Cu_3O_7$ has previously been assessed by electron structure calculations (see Pickett, 1989, and references therein). In those calculations, the reference was ions with formal valencies rather than the neutral atoms used as the reference in this presentation. In a recent study by Zhu & Taftø (1997), focusing mainly on the structure factor of the 001 reflections, it was found by comparing the experimental data with calculations for different electron-hole distribution, using a purely ionic model reference, that 76 (8)% of the holes were located in the CuO_2 planes of this fully oxygenated sample of $YBa_2Cu_3O_7$. This agrees fairly well with bond valence calculations of Brown (1991). Note that the accuracy of 8% in the determination of the hole distribution in our previous work corresponds to moving 0.08 e per crystal unit cell from the CuO_2 plane to the
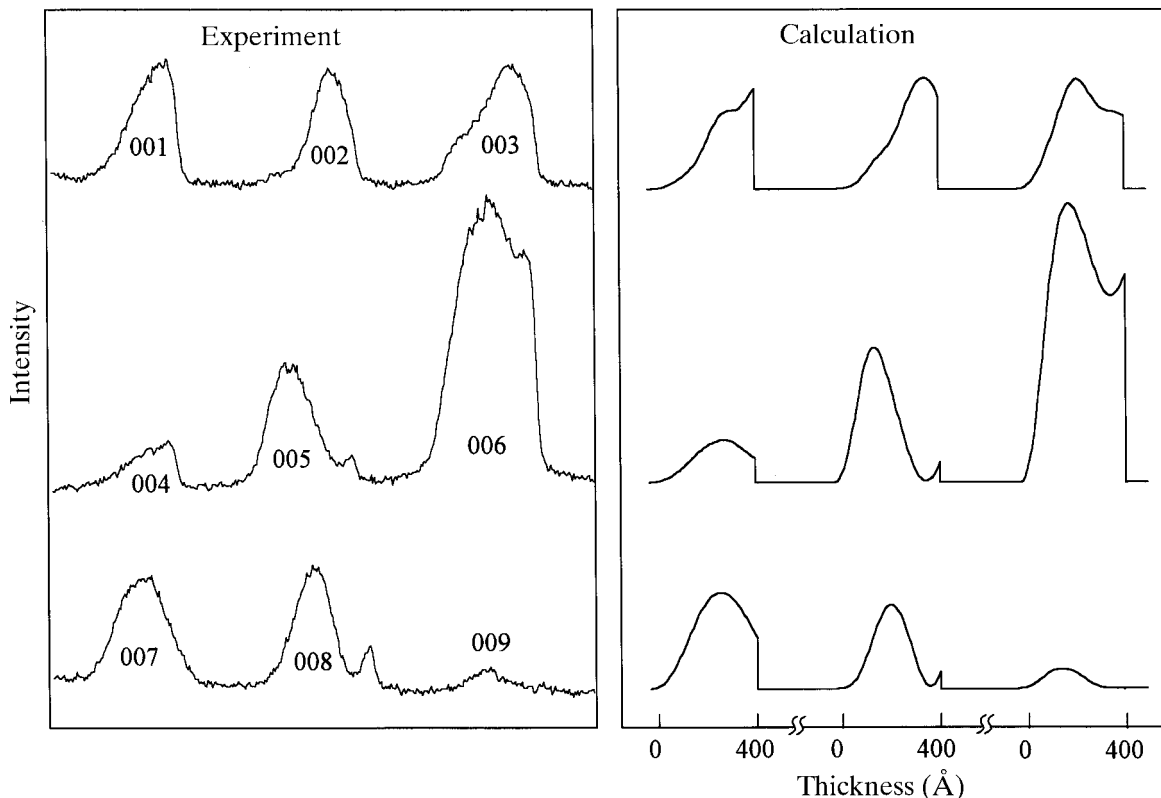

Fig. 8. Comparison between experimental intensity profiles and the one calculated for the best choice of values of the 001 and 002 structure factors. Here the 006 reflection is at the Bragg position.

CuO plane. This small change in the electron distribution significantly changes the calculated intensity profiles and, thus, demonstrates the great promise of electron diffraction in the study of valence-electron distributions in large-unit-cell crystals because this small fraction of the electrons corresponds to $0.08/294 = 0.03\%$ of the total electrons in the material.

General trends in charge transfer were obtained in this study by comparison with the expectations for neutral atoms and this can be done with rather high reliability when the atomic coordinates and occupancy are known because the scattering amplitudes of neutral atoms are known with high accuracy. When it comes to comparing with ionized atoms, we may encounter larger problems because the scattering amplitudes in that case are less accurately known and there is little consensus as to whether formal valency is a fruitful concept in this context. Thus, there is need for further efforts along these lines and the challenge has as much theoretical as experimental character for such large-unit-cell crystals where the low-order structure factors in electron diffraction are extremely sensitive to the electron charge distribution. This suggests, as a future road, a close cooperation between theoreticians doing electronic structure calculations and experimentalists.

To summarize, motivated by the challenge of determining the charge distribution of valence electrons in complex inorganic crystals, we have applied a novel approach, based on simultaneously recording the thickness fringes of many reflections in electron diffraction, to determine the structure factors of the low-order reflections in large-unit-cell crystals. With the new generation of transmission electron microscopes equipped with field emission guns, energy filters and intensity recording systems like charge-coupled-device cameras or imaging plates, this technique may be routinely applied to complex crystals. Ideal specimens are those with thin wedge-shaped areas where the thickness increases linearly with distance from the edge of the specimen. However, this technique does not rely on a perfect wedge because of the redundancy associated with recording simultaneously the thickness profiles of many reflections for the same crystallographic direction of the incident electron beam. We expect the problem of contamination to be negligible with the crossover well above or below the specimen level so that specimen regions of the order 100–1000 nm in diameter are illuminated with electrons. Thus, with an intense small electron probe at the crossover, the quality of such diffraction patterns is expected to be greatly improved.
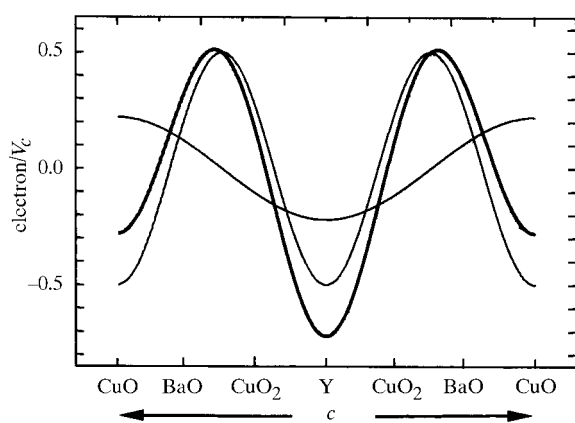
Fig. 9. Valence-electron distribution based on Fourier transform of the difference between experimental results after conversion to X-ray structure factors and the ones calculated for neutral atoms. The thin lines are the contributions from ΔF^x_{001} and ΔF^x_{002} and the thick line the sum of these two.

References

Anstis, G. R., Lynch, D. F., Moodie, A. F. & O'Keefe, M. A. (1973). *Acta Cryst.* A**29**, 138–147.

Brown, I. D. (1991). *J. Solid State Chem.* **90**, 155–167.

Burshill, L. A., Dowell, W. C. T., Goodman, P. & Tate, N. (1974). *Acta Cryst.* A**34**, 296–308.

Cherns, D., Kiely, C. J. & Preston, A. R. (1988). *Ultramicroscopy*, **24**, 355–370.

Cowley, J. M. (1953). *Acta Cryst.* **6**, 516–521, 522–529.

Duan, X. F., Cherns, D. & Steeds, J. W. (1994). *Philos. Mag.* A**70**, 1091–1105.

Gjønnes, K., Bøe, N. & Taftø, J. (1993). *Ultramicroscopy*, **48**, 37–41.

Gjønnes, J. & Høier, R. (1971). *Acta Cryst.* A**27**, 313–316.

Humphreys, C. J., Maher, D. M., Fraser, H. L. & Eaglesham, D. J. (1988). *Philos. Mag.* A**58**, 787–798.

Ichimiya, A. & Uyeda, R. (1977). *Z. Naturforsch. Teil A*, **32**, 750–753.

International Tables for Crystallography (1992). Vol. C, pp. 475–499. Dordrecht: Kluwer Academic Publishers.

Jorgensen, J. D., Veal, B. W., Paulikas, A. P., Nowicki, L. J., Crabtree, G. W., Claus, H. & Kwok, W. K. (1990). *Phys. Rev. B*, **41**, 1863–1877.

Marthinsen, K. & Høier, R. (1988). *Acta Cryst.* A**44**, 558–562.

Matsuhata, H., Gjønnes, J. & Taftø, J. (1994). *Acta Cryst.* A**50**, 115–123.

Olsen, A., Goodman, P. & Whitfield, H. J. (1985). *J. Solid State Chem.* **60**, 305–315.

Pickett, W. E. (1989). *Rev. Mod. Phys.* **61**, 433–512.

Spence, J. C. H. (1993). *Acta Cryst.* A**49**, 231–260.

Tanaka, M. (1994). *Acta Cryst.* A**50**, 261–286.

Tanaka, M., Saito, R., Ueno, K. & Harada, Y. (1980). *J. Electron Microsc.* **29**, 408–412.

Vincent, R., Bird, D. M. & Steeds, J. W. (1984). *Philos. Mag.* A**50**, 765–786.

Watanabe, D., Uyeda, R. & Fukuhara, A. (1968). *Acta Cryst.* A**24**, 580–581.

Zhu, Y. & Taftø, J. (1996). *Phys. Rev. Lett.* **76**, 443–446.

Zhu, Y. & Taftø, J. (1997). *Philos. Mag.* B**75**, 785–791.

Zuo, J. M. (1993). *Acta Cryst.* A**49**, 429–435.

Zuo, J. M., O'Keeffe, M., Rez, P. & Spence, J. C. H. (1997). *Phys. Rev. Lett.* **78**, 4777–4780.

Zuo, J. M. & Spence, J. C. H. (1991). *Ultramicroscopy*, **35**, 185–196.

Zuo, J. M., Spence, J. C. H. & Høier, R. (1989). *Phys. Rev. Lett.* **62**, 547–550.

Zuo, J. M., Spence, J. C. H. & O'Keeffe, M. (1988). *Phys. Rev. Lett.* **61**, 353–356.